


Article

Effect of Laser Pulse Width and Intensity Distribution on the Crystallographic Characteristics of GeSn Film

Xiaomeng Wang^{1,2}, Dongfeng Qi^{2,3,*}, Wenju Zhou^{1,2}, Haotian Deng^{1,2}, Yuhan Liu², Shiyong Shangguan², Jianguo Zhang², Hongyu Zheng²  and Xueyun Liu^{1,*}

¹ Laboratory of Infrared Materials and Devices, Ningbo University, Ningbo 315211, China

² Center for Advanced Laser Manufacturing, Shandong University of Technology, Zibo 255000, China

³ Laser Thermal Laboratory, Department of Mechanical Engineering, University of California, Berkeley, CA 94720-1740, USA

* Correspondence: qidongfeng@sdut.edu.cn (D.Q.); liuxueyun@nbu.edu.cn (X.L.)

Abstract: Germanium-tin (GeSn) alloy is considered a promising candidate for a Si-based short-wavelength infrared range (SWIR) detector and laser source due to its excellent carrier mobility and bandgap tunability. Pulsed laser annealing (PLA) is one of the preeminent methods for preparing GeSn crystal films with high Sn content. However, current reports have not systematically investigated the effect of different pulse-width lasers on the crystalline quality of GeSn films. In addition, the intensity of the spot follows the gaussian distribution. As a result, various regions would have different crystalline properties. Therefore, in this study, we first provide the Raman spectra of several feature regions in the ablation state for single spot processing with various pulse-width lasers (continuous-wave, nanosecond, femtosecond). Furthermore, the impact of laser pulse width on the crystallization characteristics of GeSn film is explored for different single-spot processing states, particularly the Sn content incorporated into GeSn crystals. The transient heating time of the film surface and the faster non-equilibrium transition of the surface temperature inhibit the segregation of the Sn component. By comparing the Raman spectra of the pulsed laser, the continuous-wave laser shows the most acute Sn segregation phenomenon, with the lowest Sn content of approximately 2%. However, the femtosecond laser both ensures crystallization of the film and effective suppression of Sn expulsion from the lattices, and the content of Sn is 8.07%, which is similar to the origin of GeSn film.

Keywords: laser annealing; GeSn film; pulse width; crystallographic characteristics



Citation: Wang, X.; Qi, D.; Zhou, W.; Deng, H.; Liu, Y.; Shangguan, S.; Zhang, J.; Zheng, H.; Liu, X. Effect of Laser Pulse Width and Intensity Distribution on the Crystallographic Characteristics of GeSn Film. *Coatings* **2023**, *13*, 453. <https://doi.org/10.3390/coatings13020453>

Academic Editor: Ana-Maria Lepadatu

Received: 24 January 2023

Revised: 11 February 2023

Accepted: 14 February 2023

Published: 16 February 2023



Copyright: © 2023 by the authors. Licensee MDPI, Basel, Switzerland. This article is an open access article distributed under the terms and conditions of the Creative Commons Attribution (CC BY) license (<https://creativecommons.org/licenses/by/4.0/>).

1. Introduction

As silicon (Si) is an indirect bandgap material, it has a faint Franz-Keldisch effect, a cut-off wavelength of 1.1 μm , as well as not exhibiting a linear electro-optical effect. That results in it unsuitable for direct application in photodetectors, light sources, and electro-optical modulators. Therefore, it is necessary to introduce other materials to compensate for these disadvantages [1,2]. Group III-V materials generally have excellent optoelectronic properties, but they face problems such as incompatibility with Si-based CMOS processes. Therefore, it is necessary to explore the potential of Group IV materials for optoelectronic applications. Germanium (Ge), as a CMOS compatible Group IV diamond-cubic material, has high carrier mobility [3,4]. Ge is an indirect bandgap semiconductor material, and by incorporating tin (Sn) into the Ge lattice, the gap at the Γ -point will be reduced [5,6]. And thus, a narrower bandgap can be achieved. When the content of the Sn component incorporated into Ge is greater than 10%, an indirect to direct bandgap transition will occur [7,8]. As a result, the germanium-tin (GeSn) alloy is considered a promising candidate for a Si-based short-wavelength infrared range (SWIR) detector [9,10] and laser source [6] due to its excellent carrier mobility and bandgap tunability. It also makes it possible for

Si-based monolithic photoelectric integration, on-chip laboratory [11], and expanding the working wavelength of the photodetector [9,10,12,13].

However, the low solid solubility of Sn in Ge (less than 1% at Ge-Sn eutectic temperature) makes it laborious to induce a high Sn content into GeSn crystals, resulting in Sn surface segregation [14,15]. Although non-equilibrium growth techniques such as molecular beam epitaxy (MBE) [16,17] and chemical vapor deposition (CVD) [18] have been proven to prepare the GeSn crystal films [19]. However, the lower growth temperature and the stringent growth conditions have limited their application in the optoelectronics industry. In contrast, the magnetron sputtering method is less costly and has relaxed film growth conditions, making it suitable for large-scale fabrication [13,20,21]. Furthermore, high-quality GeSn crystal films can be obtained by annealing amorphous GeSn (a-GeSn) with a high Sn content.

The annealing methods for a-GeSn films are solid-phase crystallization (SPC), rapid thermal annealing (RTA), and pulsed laser annealing (PLA) [22–24]. SPC and RTA enable the annealing of a large area of film, but the longer annealing times will induce the precipitation of large amounts of Sn components from the lattices [25]. That will have a detrimental effect on the quality of GeSn crystal films. At the same time, SPC and RTA cannot accurately anneal local surfaces. Compared with SPC and RTA, PLA can achieve high crystal quality at low processing temperatures. A shorter exposure time of the pulsed laser will induce a faster non-equilibrium transition of the surface temperature. It will enhance the content of the Sn component in the GeSn crystal films. In addition, PLA enables the annealing of specific areas of the sample, and it has also become a tool for the fabrication of periodic arrays of crystalline microstructures [26]. In recent years, several studies have reported on the crystallographic properties of RTA and PLA-treated a-GeSn films [22,26–29]. The RTA-treated films showed more severe Sn segregation. PLA is a non-equilibrium annealing method that can suppress the segregation of Sn to a certain extent. In PLA, the interaction mechanism between laser and film with different pulse widths is complex. The interaction mechanism has a significant effect on the degree of crystallization and the crystalline quality of the film. In addition, the intensity of the spot follows the Gaussian distribution, with the field intensity decreasing along the spot radius outwards. As a result, various regions in the laser spot would have different crystalline properties. However, current reports have not systematically investigated the effect of various pulse-width lasers on the crystalline quality of GeSn films, such as the content of Sn-incorporated GeSn crystals.

Therefore, in this work, we first provide the Raman spectra of different characteristic regions in the ablation state for single spot processing with various pulse-width lasers (continuous-wave, nanosecond, femtosecond). In addition, we focus on the impact of laser pulse width on the crystallization characteristics of GeSn film at different single-spot processing states, particularly the Sn content incorporated into GeSn crystals. The crystalline intensity of the GeSn crystal film and the Sn content in the GeSn crystals are both characterized using Raman spectroscopy. The frequency shift of the Raman peak and the FWHM can be used to describe how varied laser annealing pulse widths affect the Sn content incorporated into GeSn crystals. The femtosecond laser processes GeSn films with the highest Sn contents when compared with continuous-wave (CW) and nanosecond (ns) lasers. In addition, the correlation between the length of pulse width and the Sn segregation is clarified. The femtosecond (fs) laser's extremely brief pulse width and ultra-short thermal accumulation time enable rapid non-equilibrium temperature transitions at the film surface, which can more effectively suppress the segregation of Sn.

2. Material and Methods

Amorphous $\text{Ge}_{0.9}\text{Sn}_{0.1}$ (a-GeSn, the Sn content is 10%) film with a thickness of 100 nm is deposited on a SiO_2 substrate by magnetron co-sputtering techniques. The substrate samples are cleaned using the conventional RCA cleaning procedures prior to growth [30]. The substrate samples are dried with nitrogen after being rinsed in deionized water. The ionizing gas used in sputtering is argon, and the working pressure is 3.75 mTorr. The

temperature of the substrate is room temperature. The RF power of 100 W is applied to the Ge target (purity: 99.999%). The DC sputtering power ($P_{dc} = 6.8$ W) on the Sn target (purity: 99.99%) is regulated to control the Sn content to 10%. Following the completion of the material growth, scanning electron microscopy and a profilometer are used to characterize the intrinsic information of the a-GeSn film, as shown in Figure 1.

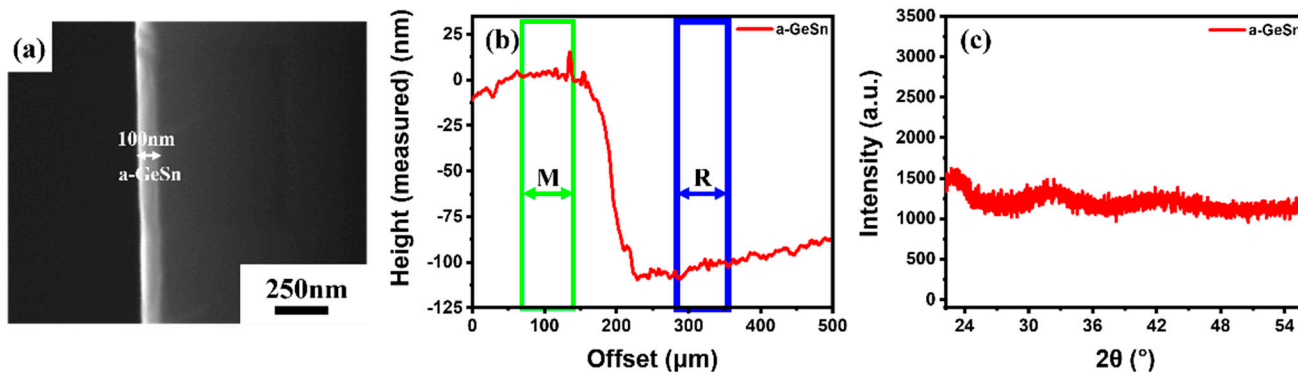


Figure 1. Intrinsic information of the a-GeSn films. (a) SEM image; (b) profilometer plots; and (c) XRD patterns.

The experimental arrangement for direct laser writing of a-Ge_{0.9}Sn_{0.1} films with different pulse widths is shown in Figure 2. The laser sources used in this research are the continuous-wave laser (CW) with the wavelength of 532 nm, Nd: YAG nanosecond laser (ns) with the center wavelength of 532 nm, the repetition rate of 10 Hz, and the pulse width of 22.5 ns (FWHM), and Ti: sapphire femtosecond laser (fs) with the center wavelength of 800 nm, the repetition rate of 1 kHz, and the pulse width of 130 fs, respectively. In the schematic diagram of the laser direct writing setup, the pulse energy is continuously regulated by adjusting the combination of a half-wave plate (HWP) and a polarized beam splitter (PBS). The laser is redirected through the mirrors, focused vertically on the surface through a 2.5× objective (NA = 0.3, Nikon, Tokyo, Japan). We use the computer to control the scanning speed of the translation stage to obtain a single pulse for processing the film surface. And the irradiation duration of the CW laser is acquired by controlling the shutter time. In addition, the process and state of laser processing are monitored by a reflective charge-coupled device (CCD) from the top view at any time.

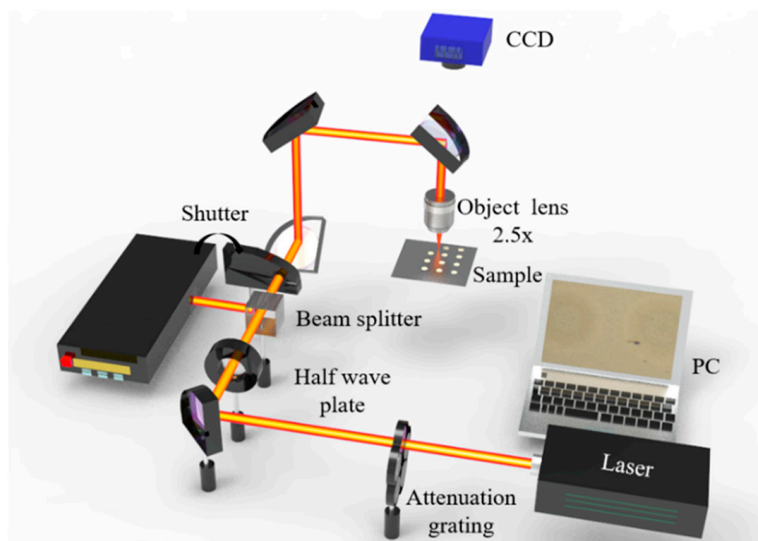


Figure 2. Schematic diagram of the device for laser direct writing of a-GeSn films with the different pulse widths (CW, ns, fs).

All experiments are performed at room temperature. The morphologies of the single-pulse action regions are characterized by the scanning electron microscope (SEM, LEO 1530, ZEISS, Jena, Germany) at an operating voltage of 20 kV. Moreover, the crystallographic characteristics of the films after laser irradiation at various pulse widths are provided by Raman microscopy (inVia, RENISHAW, Wotton-under-Edge, UK) at a wavelength of 785 nm.

3. Results and Discussion

At different pulse widths, the mechanism of laser-material interaction varies. It indicates that the surface of the sample can exhibit a variety of morphologies when exposed to laser irradiation at various pulse widths. Figure 3 shows SEM images in the crystalline, melting, and ablation states at different pulse widths.

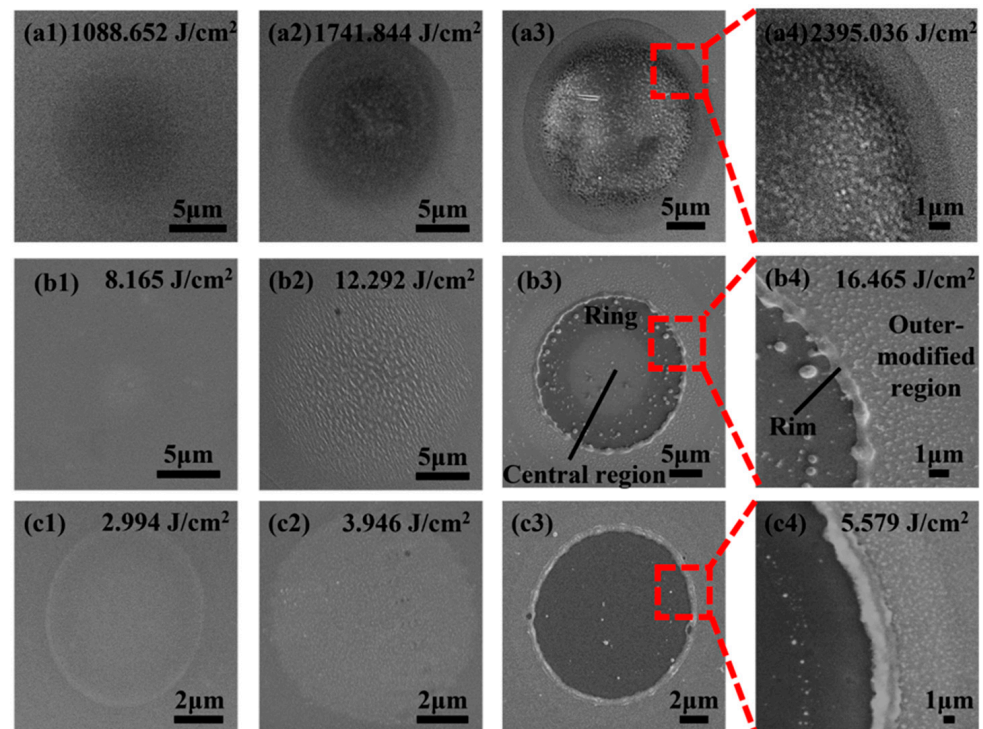


Figure 3. SEM images of the surface of the GeSn films in the crystalline, melting, and ablation states. (a1–a4) CW laser; (b1–b4) ns laser; and (c1–c4) fs laser.

After CW, ns, and fs laser irradiation, no visible grains or grain boundaries are observed on the surface of the films in the crystalline state (Figure 3(a1–c1)). The film only shows mild discoloration, suggesting that the area irradiated is modified. With increasing laser fluence, GeSn film has been beginning to melt under the CW laser irradiation, as shown in Figure 3(a2). Due to the Gaussian distribution of the spot intensity, the white flocculent crystal structures are only created at the spot's center because the film there is liquefied by the high temperature, then cooled and redistributed.

However, on the ns and fs laser-induced surfaces, the grain structures are apparent in the melting state, as shown in Figure 3(b2,c2). The size of the crystalline grain structures in the central region of ns laser irradiation is greater than that of the surrounding area, indicating that melting has been induced in the center. Rapid melting and cooling cause the material in the center to form larger grains. The melted material is de-wetted radially outward, inducing the smaller grains on the surrounding area [31]. The fs laser's non-thermal ultrafast phase transition and subsequent thermal effects cause the creation of disorganized small grains on the surface [32–34].

The ns and fs action zones are significantly ablated as the irradiation energy density rises, resulting in crater structures (Figure 3(b3,c3)). And the crystalline grain structures are present only on the outside of the crater structures. However, more areas produce white flocculent crystal structures under the CW laser irradiation (Figure 3(a3)). Besides, the intensity of the spot follows the Gaussian distribution, which means that the area of action covers a wide range of morphologies, especially the ablation state. As shown in Figure 3(b3,b4), the laser irradiation area can be divided into four typical regions (the central region, the ring region, the rim, and the outer-modified region) [35]. The droplet-like structures appear in the ring region, and the size of the droplet-like structures near the rim structure is more significant, implying melting phenomena occur in the ring region [35]. However, there are no apparent droplet-like structures inside the fs laser-induced crater, purporting that the GeSn material is directly transformed into the plasma [36].

The laser spot intensity follows the Gaussian distribution, with the field intensity decreasing along the spot radius outwards. As a result, various regions in the laser spot would have different crystalline properties. Therefore, the Raman spectra of different characteristic zones in the ablation state are examined. Figure 4 indicates the corresponding Raman spectra for different typical regions after CW, ns, and fs laser irradiation. For CW laser irradiation, the Ge-Ge mode peak ($\sim 300.4 \text{ cm}^{-1}$) [8,37] of the crystalline GeSn (c-GeSn) appears in both the center, the ring, and the out-rim region [38]. The intensity of the Raman peak decreases along the spot radius outwards. If the irradiated laser is the ns and fs, as shown in Figure 4(b1,b2,c1,c2), there is no Ge-Ge mode peak in the central region. It certifies that the material in this region is immediately ablated by the higher fluence in the center of the Gaussian spot. And the Ge-Ge mode peak appears in the outer-modified region, indicating that this region has been crystallized.

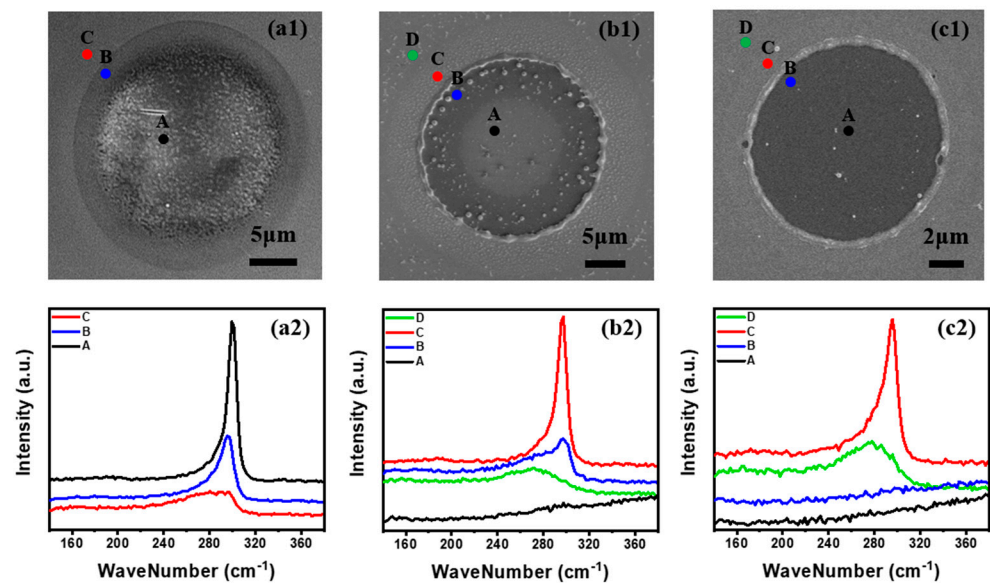


Figure 4. The corresponding Raman spectra for different regions after CW, ns, and fs laser irradiation (black for the central region, blue for the inner-rim region, and the outer-modified regions are represented by red, and green along the radius). (a1,a2) CW laser, (b1,b2) ns laser, and (c1,c2) fs laser.

The interaction mechanism between the laser and the film also varies depending on the pulse width. It not only affects the surface morphology of the film but also significantly affects its crystallographic characteristics. Therefore, Raman spectroscopy is used to investigate the impact of laser pulse width on the crystallization characteristics of GeSn film at different single-spot processing states, particularly the Sn content incorporated into GeSn crystals. Figure 5 represents the Raman spectra of the GeSn films in the laser-induced crystalline, melting, partial ablation, and ablation states, respectively. In addition, the positions of the principal peaks of crystallization are also marked in this figure.

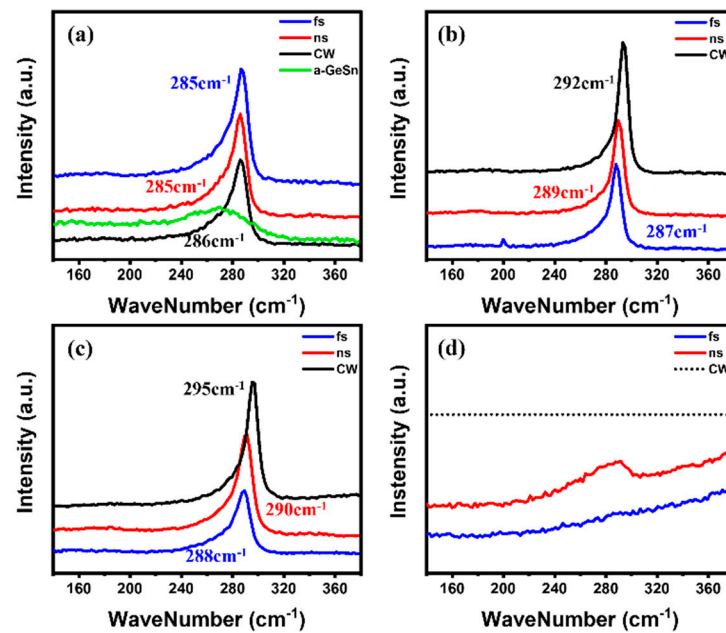


Figure 5. Raman spectra of GeSn films after laser annealing at different pulse widths. (a) Crystalline; (b) melting; (c) partial ablation; and (d) ablation states. And the positions of the principal peaks of crystallization are also marked in this figure.

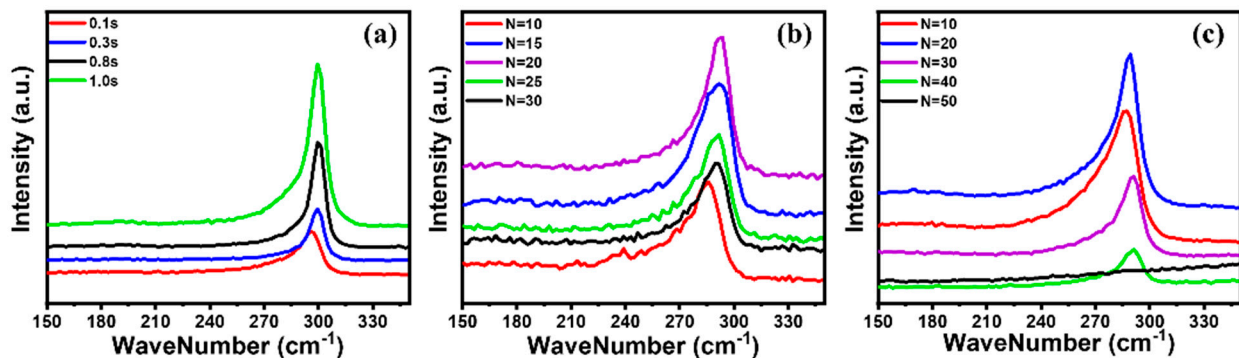
Compared with the Raman spectrum of the a-GeSn film in Figure 5a, the Raman spectrum is narrower, more intense, and blue-shifted following laser irradiation, suggesting that the film is currently beginning to crystallize. However, the Raman peak also contains a certain intensity of amorphous wave packets, as the left side of the Raman peak is more skewed than the right side. Figure 5a reveals the Raman spectra of the laser-induced crystalline state (CW, ns, and fs laser), with no significant frequency shift, and all these principal peaks are located about 285 cm^{-1} . As illustrated in Figure 5b, the peak width further reduces, the peak intensity rises, and the Raman peak is essentially symmetrical to the left and right in the laser-induced melting state, indicating a notable increase in the crystallinity of the film. In contrast to the pulsed laser (ns, fs), the CW laser's principal peak is significantly shifted toward the high wave number. Additionally, the CW laser's Raman peak exhibits a more pronounced blue shift with a peak position of 295 cm^{-1} in the partial ablation states (Figure 5c). In the ablation state, as shown in Figure 3(b3,c3), the film surface is ablated; in this case, no crystalline peaks can be detected.

The Raman shift of the crystalline peak can be attributed to the effects of the incorporation of Sn and in-plan strain and the crystal disorder impact. The peak shift ($\Delta\omega = \Delta\omega_{\text{GeSn}} - \Delta\omega_{\text{Ge}}$) can be defined as $\Delta\omega = \Delta\omega_{\text{alloy}} + \Delta\omega_{\text{strain+disorder}}$. In this equation, $\Delta\omega_{\text{alloy}} = ax$ is the Raman shift induced by the content of incorporated Sn, $a = -(82 \pm 4)$ is the coefficient [39–41]. $\Delta\omega_{\text{strain+disorder}} = -(0.6\Gamma - 3.2) \pm 0.3$ is defined as the Raman shift produced by the minimum residual amounts of strain and the disorder of the GeSn crystal [42]. In Raman scattering spectroscopy, the disorder is always related to the peak broadening, Γ is the FWHM of the GeSn crystalline peak. Therefore, the frequency shift of the Raman peak and the FWHM can be used to approximate the calculation of how varied laser annealing pulse widths affect the Sn content incorporated into GeSn crystals. Table 1 lists the calculated Sn content in the GeSn crystals and the Raman data for the GeSn films in various processing states. After CW laser or pulsed laser annealing, most of the Sn is incorporated into the crystal in its crystallized form. However, the blue shift of CW becomes more severe in the partial ablation state, and the Sn content in the crystal is just 2%, indicating that most of the Sn precipitates out [43]. In addition, the Raman spectra will shift when Sn segregation occurs during laser annealing. The blue shift of the crystalline peak becomes more pronounced the more severe the Sn segregation.

Table 1. Summary of Raman data and the content of Sn for samples after laser annealing at different pulse widths in the crystalline, melting, and partial ablation states.

Processing States	Crystalline			Melting			Partial Ablation		
	Laser Types	CW	ns	fs	CW	ns	fs	CW	ns
Raman shift (cm ⁻¹)	15.1	14.7	15.1	8.4	11.4	13.1	5.4	10.4	12.4
FWHM (cm ⁻¹)	21	20.5	20.8	12.8	13.85	16.2	12.3	15.3	18.2
The Sn content	7.3%	7.6%	8.07%	4.2%	6.9%	7.3%	2%	6.05%	6.38%

In addition, the variation of the crystalline quality of a-GeSn films under multi-pulse irradiation is also discussed, as shown in Figure 6. As the irradiation time of the CW laser increases, the intensity of the Ge-Ge mode peak enhances and then ceases to change, indicating that the film is fully crystallized at this location. However, with the increase in irradiation time, the position of the Ge-Ge mode peak has a blue shift. Furthermore, the Sn content in the GeSn crystals decreases continuously to only 1.5% after 1.0 s of laser irradiation. Unlike CW laser, the Ge-Ge mode peak has a small frequency shift after the ns and fs laser irradiation with fewer pulses. It demonstrates that the shorter laser pulse width can more effectively suppress Sn segregation. Furthermore, the fs laser ensures both the higher crystalline intensity and the higher content of the Sn component, as shown in Figure 6c in the Raman spectrum after processing with 10 shots (N = 10).

**Figure 6.** Raman spectra of the GeSn films after laser annealing at different pulse widths under the multi-pulse irradiation. (a) CW laser; (b) ns laser; and (c) fs laser.

The laser annealing process based on an extremely fast cooling rate is essentially non-thermal equilibrium processing [28,44]. However, a key factor affecting the rate of non-equilibrium transition is the length of the pulse width. The mechanism by which laser pulse width affects Sn segregation in GeSn film is illustrated by the two-temperature model (TTM), which investigates the speed of the non-equilibrium transition of the surface temperature different pulse-width laser irradiation.

$$C_e \frac{\partial}{\partial t} T_e = \exp \left[-a \frac{\tau_R}{\tau_L} \right] \frac{\partial}{\partial t} k_e \frac{\partial}{\partial x} T_e - G(T_e - T_l) + (1 - R) \alpha_b I_0(t) \exp(-\alpha_b x) \quad (1)$$

$$C_l \frac{\partial}{\partial t} T_l = G(T_e - T_l) \quad (2)$$

The TTM model is described in Equations (1) and (2). Equation (2) describes the heating of the lattice through electron-lattice coupling, with T_e and T_l representing the temperatures of electrons and lattices, and G being the electron-lattice coupling constant [45,46]. C_e and C_l are the specific heat capacities of the electrons and the lattice. $(1 - R) \alpha_b I_0(t) \exp(-\alpha_b x)$ is the radiation heating source term [47]. R is the reflectivity, and α_b is the radiation absorption coefficient. k_e is the thermal conductivity. The electronic and lattice systems inside

the system are regarded as being in thermal equilibrium when the pulse width is much greater than the electron relaxation time and the lattice thermalization time. Consequently, $T_e = T_l = T$, $\exp\left[-a\frac{\tau_R}{\tau_L}\right] \rightarrow 1$. In contrast, the PTS model can be used to represent the temperature transform process when the laser pulse width is substantially lower than the electron-phonon relaxation time, $\exp\left[-a\frac{\tau_R}{\tau_L}\right] \rightarrow 0$.

In Figure 7a, the surface temperature after ns laser irradiation with different fluences completes the transition in 200 ns, rising rapidly to the maximum and then slowly decreasing, since the pulse width of the ns laser is larger than the electron relaxation time and lattice thermalization time. Therefore, the ns laser can be considered the only heating source during the interaction between the ns laser and the GeSn film. However, the heat transfer and thermal diffusion processes of electron-lattice coupling and lattice-lattice coupling cause the surface temperature of the film to decrease slowly [48]. Therefore, the slower non-equilibrium transition of surface temperature during ns laser annealing allows the surface of the film to be heated for a long time. The accumulation and transfer of heat result in a slower cooling of the surface temperature. As a result, the accumulation and transfer of heat led to the segregation of the Sn component during this process [28].

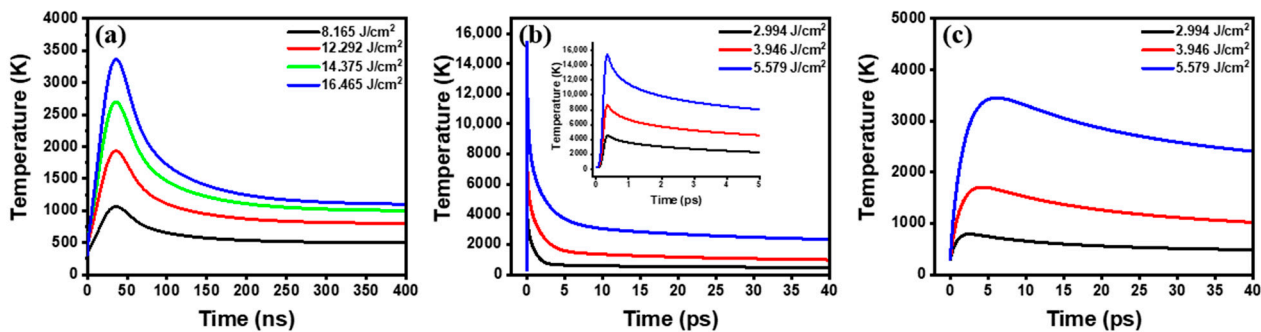


Figure 7. (a) Curves of surface temperature variation for different processing states of ns laser; (b) Curves of electron temperature variation for different processing states of fs laser; (c) Curves of lattice temperature variation for different processing states of fs laser.

Figure 7b,c show the temperature variation curves of the electrons and the lattices under the fs laser irradiation, respectively. In Figure 7c, the lattice temperature transition is complete at around 35 ps under the fs laser irradiation with the different fluence. For an fs laser, the pulse width is much smaller than the electron relaxation time. The heating is over before the electrons can transfer energy to the lattice. Therefore, the interaction of the electrons with the lattice and the heat transfer between the lattices can be ignored during the interaction of the femtosecond laser with the thin film [49]. The time for energy accumulation during fs laser processing is extremely short, and the lattice temperature can be non-equilibrium converted in the order of picoseconds.

However, the action time of the CW laser is much higher than that of the ns laser, the film is heated for a longer time, and the non-equilibrium transition in surface temperature is the slowest. When irradiated with the CW laser, the sample surface remains at a high temperature for the longest time. The sample surface can be quickly heated and cooled under fs laser irradiation. More Sn atoms can be incorporated into the Ge lattice by this non-equilibrium annealing method. Therefore, the fs pulsed laser annealing method can effectively suppress the surface Sn segregation.

We have characterized the crystallographic characteristics of GeSn films under the CW, ns, and fs-laser irradiation. Figure 8 summarizes the ratio of Sn incorporated into crystals in the crystalline, melting, and partial ablation states. As the laser fluence rises, Figure 8 shows that Sn content doped into the crystal drops. It is a result of the more intense thermal effect and slower non-equilibrium transition that occur at greater fluence, which allows for more Sn to precipitate out. Under the fs laser irradiation, the contents of the

Sn content in the crystalline, melting, and partial ablation states are 8.07%, 7.3%, and 6.38%, respectively. In the melting and partial ablation states, the Sn content incorporated into the crystals after fs laser annealing is much higher than that of the CW laser and only slightly higher than that of ns laser. With the shortest pulse width, the sample surface can be heated and cooled rapidly, and more Sn atoms can be incorporated into the Ge lattice. Therefore, thermal diffusion is not significant [49–51], and the temperature non-equilibrium transition is fast, which is more favorable for obtaining GeSn crystalline films with a higher Sn component.

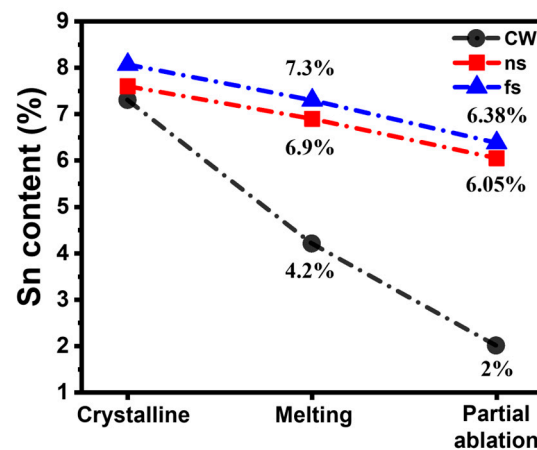


Figure 8. The content of Sn incorporated into crystals in the crystalline, melting, and partial ablation states.

4. Conclusions

In conclusion, we have examined how the laser pulse width affects the crystallographic characteristics of a-GeSn films in the crystalline, melting, partial ablation, and ablation states, particularly on the issue of Sn segregation. Using Raman spectroscopy to correlate the frequency shift of the Ge-Ge mode peaks with Sn segregation, the crystalline quality of the GeSn film is evaluated. The fs laser processes GeSn films with the highest Sn ratios compared with the CW and ns lasers. From the perspective of the temperature transition at the film surface, the two-temperature model (TTM) is utilized to describe the mechanism of the laser pulse width on the Sn segregation. After fs laser irradiation, more Sn can be incorporated into crystalline GeSn from the amorphous GeSn, which is attributed to the rapid non-equilibrium temperature transitions. Therefore, the fs laser annealing method can effectively suppress Sn segregation, which is an effective annealing method for obtaining GeSn films with high Sn contents.

Author Contributions: Software, W.Z.; Validation, X.W. and W.Z.; Formal analysis, X.W.; Investigation, H.D., Y.L., S.S., J.Z., H.Z. and X.L.; Writing—original draft, X.W.; Writing—review and editing, X.W., D.Q., H.Z. and X.L.; Supervision, D.Q.; Project administration, D.Q. All authors have read and agreed to the published version of the manuscript.

Funding: This work was supported by the National Key R&D Program of China, 2022YFE0199100; Natural Science Foundation of Shandong (ZR2021MF030); Natural Science Foundation of Zhejiang (LY21F050002); (2022TSGC1159).

Institutional Review Board Statement: Not applicable.

Informed Consent Statement: Not applicable.

Data Availability Statement: Data sharing is not applicable to this article.

Conflicts of Interest: The authors declare no conflict of interest.

References

1. Tomioka, K.; Motohisa, J.; Hara, S.; Hiruma, K.; Fukui, T. GaAs/AlGaAs core multishell nanowire-based light-emitting diodes on Si. *Nano Lett.* **2010**, *10*, 1639–1644. [[CrossRef](#)]
2. Gupta, S.; Magyari-Köpe, B.; Nishi, Y.; Saraswat, K.C. Achieving direct band gap in germanium through integration of Sn alloying and external strain. *J. Appl. Phys.* **2013**, *113*, 073707. [[CrossRef](#)]
3. Yang, Y.; Wang, X.; Wang, C.; Song, Y.; Zhang, M.; Xue, Z.; Wang, S.; Zhu, Z.; Liu, G.; Li, P.; et al. Ferroelectric enhanced performance of a GeSn/Ge dual-nanowire photodetector. *Nano Lett.* **2020**, *20*, 3872–3879. [[CrossRef](#)] [[PubMed](#)]
4. Wirths, S.; Buca, D.; Mantl, S. Si–Ge–Sn alloys: From growth to applications. *Prog. Cryst. Growth Charact. Mater.* **2016**, *62*, 1–39. [[CrossRef](#)]
5. Jenkins, D.W.; Dow, J.D. Electronic properties of metastable $\text{Ge}_x\text{Sn}_{1-x}$ alloys. *Phys. Rev. B* **1987**, *36*, 7994. [[CrossRef](#)] [[PubMed](#)]
6. Wirths, S.; Geiger, R.; Von Den Driesch, N.; Mussler, G.; Stoica, T.; Mantl, S.; Ikonic, Z.; Luysberg, M.; Chiussi, S.; Hartmann, J.-M. Lasing in direct-bandgap GeSn alloy grown on Si. *Nat. Photonics* **2015**, *9*, 88–92. [[CrossRef](#)]
7. Biswas, S.; Doherty, J.; Saladukha, D.; Ramasse, Q.; Majumdar, D.; Upmanyu, M.; Singha, A.; Ochalski, T.; Morris, M.A.; Holmes, J.D. Non-equilibrium induction of tin in germanium: Towards direct bandgap $\text{Ge}_{1-x}\text{Sn}_x$ nanowires. *Nat. Commun.* **2016**, *7*, 11405. [[CrossRef](#)]
8. Mahmodi, H.; Hashim, M.; Hashim, U. Formation of nanocrystalline GeSn thin film on Si substrate by sputtering and rapid thermal annealing. *Superlattices Microstruct.* **2016**, *98*, 235–241. [[CrossRef](#)]
9. Meng, A.C.; Fenrich, C.S.; Braun, M.R.; McVittie, J.P.; Marshall, A.F.; Harris, J.S.; McIntyre, P.C. Core-shell germanium/germanium–tin nanowires exhibiting room-temperature direct-and indirect-gap photoluminescence. *Nano Lett.* **2016**, *16*, 7521–7529. [[CrossRef](#)]
10. Seifner, M.S.; Dijkstra, A.; Bernardi, J.; Steiger-Thirsfeld, A.; Sistani, M.; Lugstein, A.; Haverkort, J.E.; Barth, S. Epitaxial $\text{Ge}_0.81\text{Sn}_0.19$ nanowires for nanoscale mid-infrared emitters. *ACS Nano* **2019**, *13*, 8047–8054. [[CrossRef](#)]
11. Soref, R. Mid-infrared photonics in silicon and germanium. *Nat. Photonics* **2010**, *4*, 495–497. [[CrossRef](#)]
12. Assali, S.; Dijkstra, A.; Li, A.; Koelling, S.; Verheijen, M.; Gagliano, L.; Von Den Driesch, N.; Buca, D.; Koenraad, P.; Haverkort, J. Growth and optical properties of direct band gap Ge/Ge_{0.87}Sn_{0.13} core/shell nanowire arrays. *Nano Lett.* **2017**, *17*, 1538–1544. [[CrossRef](#)] [[PubMed](#)]
13. Dascalescu, I.; Zoita, N.C.; Slav, A.; Matei, E.; Iftimie, S.; Comanescu, F.; Lepadatu, A.-M.; Palade, C.; Lazanu, S.; Buca, D. Epitaxial GeSn obtained by high power impulse magnetron sputtering and the heterojunction with embedded GeSn nanocrystals for shortwave infrared detection. *ACS Appl. Mater. Interfaces* **2020**, *12*, 33879–33886. [[CrossRef](#)] [[PubMed](#)]
14. Thurmond, C.; Trumbore, F.; Kowalchik, M. Germanium solidus curves. *J. Chem. Phys.* **1956**, *25*, 799–800. [[CrossRef](#)]
15. Fleurial, J.P.; Borshchevsky, A. Si-Ge-metal ternary phase diagram calculations. *J. Electrochem. Soc.* **1990**, *137*, 2928. [[CrossRef](#)]
16. Zhang, D.; Jin, L.; Li, J.; Wen, T.; Liu, C.; Xu, F.; Kolodzey, J.; Liao, Y. MBE growth of ultra-thin GeSn film with high Sn content and its infrared/terahertz properties. *J. Alloys Compd.* **2016**, *665*, 131–136. [[CrossRef](#)]
17. Richard D’Costa, V.; Wang, W.; Zhou, Q.; Soon Tok, E.; Yeo, Y.-C. Above-bandgap optical properties of biaxially strained GeSn alloys grown by molecular beam epitaxy. *Appl. Phys. Lett.* **2014**, *104*, 022111. [[CrossRef](#)]
18. Dou, W.; Benamara, M.; Mosleh, A.; Margetis, J.; Grant, P.; Zhou, Y.; Al-Kabi, S.; Du, W.; Tolle, J.; Li, B. Investigation of GeSn strain relaxation and spontaneous composition gradient for low-defect and high-Sn alloy growth. *Sci. Rep.* **2018**, *8*, 5640. [[CrossRef](#)]
19. Conley, B.R.; Mosleh, A.; Ghetmiri, S.A.; Du, W.; Soref, R.A.; Sun, G.; Margetis, J.; Tolle, J.; Naseem, H.A.; Yu, S.-Q. Temperature dependent spectral response and detectivity of GeSn photoconductors on silicon for short wave infrared detection. *Opt. Express* **2014**, *22*, 15639–15652. [[CrossRef](#)]
20. Zheng, J.; Li, L.; Zhou, T.; Zuo, Y.; Li, C.; Cheng, B.; Wang, Q. Growth of crystalline $\text{Ge}_{1-x}\text{Sn}_x$ films on Si (100) by magnetron sputtering. *Solid-State Lett.* **2014**, *3*, P111. [[CrossRef](#)]
21. Slav, A.; Dascalescu, I.; Lepadatu, A.-M.; Palade, C.; Zoita, N.C.; Stroescu, H.; Iftimie, S.; Lazanu, S.; Gartner, M.; Buca, D. GeSn/SiO₂ multilayers by magnetron sputtering deposition for short-wave infrared photonics. *ACS Appl. Mater. Interfaces* **2020**, *12*, 56161–56171. [[CrossRef](#)] [[PubMed](#)]
22. Sakaike, K.; Higashi, S.; Murakami, H.; Miyazaki, S. Crystallization of amorphous Ge films induced by semiconductor diode laser annealing. *Thin Solid Film.* **2008**, *516*, 3595–3600. [[CrossRef](#)]
23. Chikita, H.; Matsumura, R.; Kai, Y.; Sadoh, T.; Miyao, M. Ultra-high-speed lateral solid phase crystallization of GeSn on insulator combined with Sn-melting-induced seeding. *Appl. Phys. Lett.* **2014**, *105*, 202112. [[CrossRef](#)]
24. Zheng, J.; Liu, Z.; Zhang, Y.; Zuo, Y.; Li, C.; Xue, C.; Cheng, B.; Wang, Q. Growth of high-Sn content (28%) GeSn alloy films by sputtering epitaxy. *J. Cryst. Growth* **2018**, *492*, 29–34. [[CrossRef](#)]
25. Slav, A.; Palade, C.; Logofatu, C.; Dascalescu, I.; Lepadatu, A.M.; Stavarache, I.; Comanescu, F.; Iftimie, S.; Antohe, S.; Lazanu, S. GeSn nanocrystals in GeSnSiO₂ by magnetron sputtering for short-wave infrared detection. *ACS Appl. Nano Mater.* **2019**, *2*, 3626–3635. [[CrossRef](#)]
26. Mulato, M.; Toet, D.; Aichmayr, G.; Spangenberg, A.; Santos, P.; Chambouleyron, I. Short-pulse laser crystallization and structuring of a-Ge. *J. Non-Cryst. Solids* **1998**, *227*, 930–933. [[CrossRef](#)]
27. Von Den Driesch, N.; Stange, D.; Wirths, S.; Mussler, G.; Hollander, B.; Ikonic, Z.; Hartmann, J.; Stoica, T.; Mantl, S.; Grützmacher, D. Direct bandgap group IV epitaxy on Si for laser applications. *Chem. Mater.* **2015**, *27*, 4693–4702. [[CrossRef](#)]
28. Moto, K.; Matsumura, R.; Sadoh, T.; Ikenoue, H.; Miyao, M. Pulse number controlled laser annealing for GeSn on insulator structure with high substitutional Sn concentration. *Appl. Phys. Lett.* **2016**, *108*, 262105. [[CrossRef](#)]

29. Yoshikawa, I.; Kurosawa, M.; Takeuchi, W.; Sakashita, M.; Nakatsuka, O.; Zaima, S. Low-temperature crystallization of Ge-rich GeSn layers on Si₃N₄ substrate. *Mater. Sci. Semicond. Process.* **2017**, *70*, 151–155. [[CrossRef](#)]
30. Hong, H.; Zhang, L.; Qian, K.; An, Y.; Li, C.; Li, J.; Chen, S.; Huang, W.; Wang, J.; Zhang, S. Limitation of bulk GeSn alloy in the application of a high-performance laser due to the high threshold. *Opt. Express* **2021**, *29*, 441–453. [[CrossRef](#)]
31. Qi, D.; Zhang, Z.; Yu, X.; Zhang, Y. Visualization of nanosecond laser-induced dewetting, ablation and crystallization processes in thin silicon films. *Phys. Lett. A* **2018**, *382*, 1540–1544. [[CrossRef](#)]
32. Von der Linde, D.; Fabricius, N. Observation of an electronic plasma in picosecond laser annealing of silicon. *Appl. Phys. Lett.* **1982**, *41*, 991–993. [[CrossRef](#)]
33. Choi, T.Y.; Hwang, D.J.; Grigoropoulos, C.P. Ultrafast laser-induced crystallization of amorphous silicon films. *Opt. Eng.* **2003**, *42*, 3383–3388.
34. Amoruso, S.; Ausanio, G.; Bruzzese, R.; Vitiello, M.; Wang, X. Femtosecond laser pulse irradiation of solid targets as a general route to nanoparticle formation in a vacuum. *Phys. Rev. B* **2005**, *71*, 033406. [[CrossRef](#)]
35. Bonse, J.; Wrobel, J.; Brzezinka, K.-W.; Esser, N.; Kautek, W. Femtosecond laser irradiation of indium phosphide in air: Raman spectroscopic and atomic force microscopic investigations. *Appl. Surf. Sci.* **2002**, *202*, 272–282. [[CrossRef](#)]
36. Wang, Q.; Jiang, L.; Sun, J.; Pan, C.; Han, W.; Wang, G.; Wang, F.; Zhang, K.; Li, M.; Lu, Y. Structure-mediated excitation of air plasma and silicon plasma expansion in femtosecond laser pulses ablation. *Research* **2018**, *2018*, 5709748. [[CrossRef](#)] [[PubMed](#)]
37. Dos Santos, D.; Torriani, I. Crystallite size determination in $\mu\text{-Ge}$ films by X-ray diffraction and Raman line profile analysis. *Solid State Commun.* **1993**, *85*, 307–310. [[CrossRef](#)]
38. Stefanov, S.; Conde, J.; Benedetti, A.; Serra, C.; Werner, J.; Oehme, M.; Schulze, J.; Chiussi, S. Laser assisted formation of binary and ternary Ge/Si/Sn alloys. *Thin Solid Films* **2012**, *520*, 3262–3265. [[CrossRef](#)]
39. Lin, H.; Chen, R.; Huo, Y.; Kamins, T.I.; Harris, J.S. Raman study of strained Ge_{1-x}Sn_x alloys. *Appl. Phys. Lett.* **2011**, *98*, 261917. [[CrossRef](#)]
40. D’costa, V.; Tolle, J.; Roucka, R.; Poweleit, C.; Kouvetakis, J.; Menendez, J. Raman scattering in Ge_{1-y}Sn_y alloys. *Solid State Commun.* **2007**, *144*, 240–244. [[CrossRef](#)]
41. Zhang, L.; Wang, Y.; Chen, N.; Lin, G.; Li, C.; Huang, W.; Chen, S.; Xu, J.; Wang, J. Raman scattering study of amorphous GeSn films and their crystallization on Si substrates. *J. Non-Cryst. Solids* **2016**, *448*, 74–78. [[CrossRef](#)]
42. Zhang, L.; Hong, H.-Y.; Wang, Y.-S.; Li, C.; Lin, G.-Y.; Chen, S.-Y.; Huang, W.; Wang, J.-Y. Formation of high-Sn content polycrystalline GeSn films by pulsed laser annealing on co-sputtered amorphous GeSn on Ge substrate. *Chin. Phys. B* **2017**, *26*, 116802. [[CrossRef](#)]
43. Su, S.; Wang, W.; Cheng, B.; Hu, W.; Zhang, G.; Xue, C.; Zuo, Y.; Wang, Q. The contributions of composition and strain to the phonon shift in Ge_{1-x}Sn_x alloys. *Solid State Commun.* **2011**, *151*, 647–650. [[CrossRef](#)]
44. Hatano, M.; Moon, S.; Lee, M.; Suzuki, K.; Grigoropoulos, C.P. Excimer laser-induced temperature field in melting and resolidification of silicon thin films. *J. Appl. Phys.* **2000**, *87*, 36–43. [[CrossRef](#)]
45. Qiu, T.; Tien, C. Femtosecond laser heating of multi-layer metals—I. Analysis. *Int. J. Heat Mass Transf.* **1994**, *37*, 2789–2797. [[CrossRef](#)]
46. Zhang, Q.; Huang, D.; Qi, D.; Zhou, W.; Wang, L.; Zhang, Z.; Chen, S.; Dai, S.; Zheng, H. Mask-free patterning of Cu mesh as smart windows by spatially modulated nanosecond laser pulses. *Opt. Laser Technol.* **2021**, *140*, 107056. [[CrossRef](#)]
47. Qiu, T.; Tien, C. Heat transfer mechanisms during short-pulse laser heating of metals. *J. Heat Transf.* **1993**, *115*, 835–841. [[CrossRef](#)]
48. Chen, M.; Wang, X.; Qi, D.; Deng, H.; Liu, Y.; Shen, X. Temperature field simulation of chalcogenide glass ablation by nanosecond pulsed laser-based on pump-probe technology. *Opt. Laser Technol.* **2022**, *149*, 107771. [[CrossRef](#)]
49. Wang, H.; Qi, D.; Yu, X.; Zhang, Y.; Zhang, Z.; Xu, T.; Zhang, X.; Dai, S.; Shen, X.; Song, B. In-situ and ex-situ characterization of femtosecond laser-induced ablation on As₂S₃ chalcogenide glasses and advanced grating structures fabrication. *Materials* **2018**, *12*, 72. [[CrossRef](#)]
50. Xiao, C.; Song, B.; Jin, Y.; Zhang, X.; Lin, C.; Zhang, P.; Dai, S. Study on the factors affecting the refractive index change of chalcogenide films induced by femtosecond laser. *Opt. Laser Technol.* **2019**, *120*, 105708. [[CrossRef](#)]
51. Zhang, D.; Wu, L.-C.; Ueki, M.; Ito, Y.; Sugioka, K. Femtosecond laser shockwave peening ablation in liquids for hierarchical micro/nanostructuring of brittle silicon and its biological application. *Int. J. Extrem. Manuf.* **2020**, *2*, 045001. [[CrossRef](#)]

Disclaimer/Publisher’s Note: The statements, opinions and data contained in all publications are solely those of the individual author(s) and contributor(s) and not of MDPI and/or the editor(s). MDPI and/or the editor(s) disclaim responsibility for any injury to people or property resulting from any ideas, methods, instructions or products referred to in the content.